Enhancing $Ce_xZr_{1-x}O_2$ Activity for Methane Dry Reforming Using Subsurface Ni Dopants

Behnam Safavinia,[a] Yuming Wang,[a] Changyi Jiang,[a] Cameron Roman[a], Pragathi Darapaneni,[a] Jarod Larriviere,[a] David A. Cullen,[b] Kerry M. Dooley,[a] James A. Dorman[,a]*

[a] Cain Department of Chemical Engineering, Louisiana State University, Baton Rouge, Louisiana 70803, United States

[b]Center for Nanophase Materials Sciences, Oak Ridge National Laboratory, Oak Ridge, Tennessee 37831, United States

KEYWORDS: *Raman spectroscopy, Nanoparticles, Oxygen vacancies, Cerium zirconium oxide, Catalyst, Methane Dry Reforming*

§ *Supporting Information*

ABSTRACT: CeO_2-ZrO_2 (CZO) nanoparticles (NPs) have application in many catalytic reactions, such as methane dry reforming, due to their oxygen cycling ability. Ni doping has been shown to improve the catalytic activity and produces active sites for the decomposition of methane. In this work, Ni:CZO NPs were synthesized via a two-step co-precipitation/molten salt synthesis to compare Ni distribution, oxygen vacancy concentration, and catalytic activity relative to a reference state-of-the-art catalyst prepared by a sol-gel-adsorptive deposition technique. To better understand the dispersion of Ni and oxygen vacancy formation in these materials, the Ni concentration, position, and reaction time were varied in the synthesis. X-ray diffraction (XRD)

measurements show a homogeneous, cubic phase with little to no segregation of Ni/NiO. Catalytic activity measurements, performed via a DSC/TGA method, displayed a five-fold increase in activity per surface area with an order of magnitude decrease in the coking rate for the particles synthesized by the molten salt method. Additionally, this approach resulted in an order of magnitude increase in oxygen vacancies which is attributed to the high dispersion of Ni^{2+} ions in the NP core. This ability to control the oxygen vacancies in the lattice is expected to impact other such systems which utilize the substrate redox cyclability to drive conversion via (e.g.) a Mars-van Krevelen mechanism.

1. INTRODUCTION

One of the major problems faced in Ni-doped CeO_2-ZrO_2 (CZO) catalysts is sintering and coke formation at dry reforming of methane (DRM) operating conditions, 650-850 °C and 1-10 atm.[1-4] Homogeneously dispersing the active sites over the surface of the catalyst has been shown to prevent coking, because of the absence of faceted Ni surfaces.[2, 5-10] Alternatively, coke formation is reduced on materials with high oxygen storage capacities (OSC) due to lattice oxygen interactions with adsorbed carbon moieties. The OSC of CZO is known to be a function of the Zr concentration, peaking at around 30 mol% Zr.[11-18] As such, cerium-based catalysts have been used in a variety of lattice oxygen-mediated catalytic reactions, e.g., three-way exhaust catalysis[19], dry(tri) reforming of methane[20, 21], water-gas shift reactions[22] and others[12]. Additionally, other transition metals (Pd, Pt, Rh, Mn, etc.) have been studied in combination with the CZO substrate to lower reaction onset temperatures, along with other effects.[23-29] However, with all these materials there is the synthetic challenge to maximize the OSC and active site dispersion while maintaining catalyst stability with respect to both metal ripening and coking. One relatively

unexplored approach is the subsurface incorporation of the Ni dopant to increase internal strain without the formation of faceted islands.

Accordingly, there is a large body of literature on the preparation of CZO NPs using various synthetic methods such as sol-gel[30, 31], coprecipitation[9], flame-made[32], etc. which yield different oxygen vacancy concentrations despite containing identical compositions.[33-36] To achieve an ideal Ce:Zr ratio of ~2:1 for maximum OSC the synthetic conditions must be carefully controlled to ensure local and long-range homogeneity due to the different formation rates of the oxides.[2, 6, 37] Additionally, post-processing techniques (e.g., strong electrostatic adsorption or incipient wetness impregnation) are often used to activate the catalysts with Ni. However, high temperatures and oxidative/reducing atmospheres can lead to structural changes and reduced OSC.[10, 38] Specifically, exposure to reducing atmospheres often leads to the formation of segregated CeO_2 and ZrO_2, and non-uniform distribution of Ni.[10] This process results in larger Ni clusters that can facilitate dendrite formation and rapid deactivation of the catalyst.[9, 10, 39] Therefore, alternative methods are needed to synthesize activated nanoparticles that are less susceptible to oxide segregation and Ni island formation.

To address this, others have incorporated Ni salts (up to 15 mol%) during the Ce-Zr-O co-precipitation process prior to a high-temperature sintering step, producing Ni cluster sizes of ~12 nm on the catalyst surface.[2] However, with this method it is difficult to spatially control the Ni during incorporation in the bulk of the catalyst and to correlate the role of Ni to the OSC of the catalyst.[40] On the other hand, a two-step co-precipitation (CP)/molten salt synthesis (MSS) method has been reported which facilitates the incorporation of dopants within complex metal oxides (below the surface) during synthesis.[41-45] By precipitating the precursors from an aqueous solution in the initial step, M-O-M bonds are formed which then undergo reorganization during the high-

temperature treatment to solidify the structure.[46, 47] The formation of the disorganized initial structure results in enhanced phase stability and facilitates the incorporation of a homogenously distributed dopant.[48, 49] Modification of this reported two-step process will allow for controlled Ni distribution in CZO catalysts and for the elucidation of the effects of oxygen mobility/concentration and active site location on catalyst stability, activity, and coking.

In this work, Ni:CZO NPs are prepared by a two-step synthesis, CP followed by MSS, to create a highly dispersed disordered fluorite phase with increased oxygen vacancies. This method allows for production of structure-controlled NPs where the oxygen vacancies can be modified by varying precursor compositions and reaction time. The oxygen vacancy concentration and catalytic activity of the Ni:CZO NPs prepared via CP/MSS were then compared to a more conventional state-of-the-art catalyst prepared via the sol-gel technique. Structural and chemical characterizations were performed on the synthesized NPs to determine the morphology, stoichiometry, and chemical composition prior to any catalytic reaction tests. The percentage of Ni was systematically varied up to 20 mol% to identify the optimum Ni content for catalytic activity in dry reforming of methane (DRM) and oxygen vacancy concentration. Thermogravimetric analysis (DSC/TGA), Raman spectroscopy, and X-ray photoelectron spectroscopy (XPS) were performed to determine the catalytic activity, Ce oxidation state, and oxygen vacancy concentrations of the NPs. The ability to spatially distribute the Ni within the catalyst resulted in a near five-fold increase in activity per surface area and an order of magnitude decrease in coking, suggesting that subsurface active sites play an important role in catalytic activity of methane reforming reactions. While this work only includes a single dopant (Ni), this process can be used to control dopant distribution of multiple types.[50, 51]

2. EXPERIMENTAL SECTION

Materials. Cerium (III) nitrate hexahydrate ($Ce(NO_3)_3 \cdot 6H_2O$, Strem Chemicals, 99.9%), ammonium cerium nitrate $(NH_4)_2Ce(NO_3)_6$ (98+%, Alfa), zirconium oxynitrate hydrate ($ZrO(NO_3)_2 \cdot xH_2O$, Beantown Chemical, 99.9%), nickel chloride hexahydrate ($NiCl_2.6H_2O$, Beantown Chemical, 99.0%), 28-30% ammonium hydroxide (NH_4OH, VWR Chemicals, ACS grade) and urea (CH_4N_2O, VWR Chemicals, ACS grade) were used for the synthesis. $NaNO_3$ (high purity grade, VWR Chemicals), and KNO_3 (ACS grade, VWR Chemicals) were utilized for the molten salt synthesis. Hydrochloric acid (HCl, 36.5-38%, VWR Chemicals) and nitric acid (HNO_3, 68-70%, VWR Chemicals) were used for the ICP-OES digestion process.

Preparation of Ni:CZO NPs. Particles were prepared using a two-step, CP/MSS process.[41-44, 52] The CP was performed by dissolving a 2:1 Ce:Zr molar ratio of $Ce(NO_3)_3 \cdot 6H_2O$:$ZrO(NO_3)_2 \cdot xH_2O$ in 400 mL of deionized (DI) water. Ni was incorporated by adding up to 20 mol% of $NiCl_2 \cdot 6H_2O$ in the solution. Actual doping concentrations are reported in Table S1. The pH of the solution was adjusted dropwise with 28% NH_4OH resulting in a pH of ~11. The solution was stirred for 2 h and the resultant powder was collected through vacuum filtration and washed with DI water until the supernatant was neutral.[53] The resultant powder was dried at 90 ºC overnight. In the second step, 700 mg of the as-prepared single-source complex precursor was mixed with a eutectic salt mixture (e.g. $NaNO_3$:KNO_3 = 1:1, molar ratio), transferred to a porcelain crucible, and heated at 650 ℃ with a 10 ℃/min ramp rate. The reaction was allowed to occur for up to 6 h. The resulting solution was cooled naturally to room temperature and the salt crystal dissolved in DI water. After complete dissolution of the salts, the powder was centrifuged and washed 5 times with DI water to completely remove excess salts. The particles were then collected and dried overnight at 90 ℃. For the synthesis of the core-shell NPs, the core was synthesized via the above CP/MSS synthesis and the shell was added by adsorptive deposition[54, 55]. The core NPs along with $NiCl_2 \cdot 6H_2O$ were

added to 20 mL of 0.3M of urea and was refluxed for 24 h. After filtering and washing the powders, the sample was reduced in 5% H_2/95% Ar (300 mL/min) for 6 h at 750 °C. The reference catalyst was prepared by a templated sol-gel method followed by a deposition-precipitation step.[54] The precursors $(NH_4)_2Ce(NO_3)_6$ and $ZrO(NO_3)_2$ were dissolved in 96% water/3% methanol/ 1% TMAOH surfactant (25% in methanol). The pH was adjusted to 10.3 by gradually adding the ammonia solution and the solution reacted for 2 days at 90 °C. After washing of the sol-gel with DI water, the mixed oxide was dried at 120 °C overnight and calcined in air for 6 h. To deposit the Ni active by adsorptive deposition, the mixed oxide and $Ni(NO_3)_2 \cdot 6H_2O$ (Aldrich, reagent) was added to 0.3 M urea and reacted for 24 h at 90 °C. After washing and drying (same as above) was performed, the catalyst was reduced in 5% H_2/N_2 at 750 °C for 6 h.

Structural characterization. All structural characterizations were performed prior to the reduction treatment unless noted in the text. The crystal structure was identified via powder X-ray diffraction (XRD) using PANalytical X-ray diffractometer at 45 kV and 40 mA. The θ-2θ radial scan was performed over the range 5-70º with a step size of 0.04º and dwell time of 60 s, using Cu K_α (λ=1.54 Å) as radiation source. The morphology and size of Ni:CZO NPs were confirmed by high-resolution transmission electron microscopy (HRTEM) using a 200 kV JEOL NEARM electron microscope equipped with double aberration correctors, a dual-energy-loss spectrometer, and a cold FEG source. The powder sample was dispersed in ethanol and drop casted on a 300 mesh, lacey carbon grid prior to imaging. Specific surface area (BET) measurements were carried out in a Micromeritics ASAP-2020 porosimeter (three points). The elemental composition of the NPs was measured using a PerkinElmer Optima 8000 ICP-OES spectrometer.

Raman spectra were measured using a Renishaw inVia Reflex Raman Spectrometer with a 0.1 mW diode laser at an excitation wavelength of 532 nm, exposure time of 0.5 s, spectral resolution of 1 cm^{-1} and ~5 μm spot size.

XPS measurements were performed using a Scienta Omicron ESCA 2SR equipped with a monochromatic Al K_α (hν=1486.6 eV) X-ray source and a hemispherical analyzer with a 128-channel detector, at 1.3×10^{-9} torr. The Gaussian width of the photon source was 0.5 eV and a focus voltage of 300 V. The XPS spectra were calibrated to the adventitious C 1*s* peak at 285.7 eV. All peaks were fit (using CasaXPS software[56]) as Gaussians after Shirley background subtraction.

CO chemisorption was performed to verify the active site dispersion (Ni/NiO) on the surface of the catalyst. 500 mg of the catalyst was loaded and pretreated in 5% H_2/95% N_2 overnight. CO pulse chemisorption (Micromeritics 2700) at various temperatures was measured after purging the surface with N_2. TPR was performed by reduction of pre-oxidized (500 °C, 1 h, air) samples in the DSC/TGA. The samples were reduced at 10 °C/min from 50 to 1000 °C in 5% H_2/N_2. They were then re-oxidized at 500°C to check for weight recovery.

Catalytic performance evaluation. The coking rate and catalytic activity were measured using a Differential Scanning Calorimetry (DSC)/Thermogravimetric Analyzer (TGA) (TA SDT Q600). The catalyst was activated in air overnight at 750 °C. The DRM reaction was performed at 750 °C and 135 mL/min total flow rate (1:1 CH_4:CO_2, 0.25 atm partial pressure of each, with 0.50 atm N_2). The heat flux and change in mass were both measured, the former being proportional to the endothermic heat of the DRM reaction while the latter being proportional to the coking rate. The reforming rate was extracted from the heat effect using an Aspen HYSYS model of the process.

To scale up the DSC/TGA measurement, selected catalysts were tested in a fixed-bed reactor. The fixed bed reactor is a 1/2" stainless steel reactor tube with α-alumina and 0.25 g of catalyst. The DRM performed in this reactor contains higher partial pressures for CO_2 and CH_4 (~0.65 atm each) than the DSC/TGA measurements.

3. RESULTS AND DISCUSSION

The 2:1 Ce:Zr mixed oxide and a 6.6 mol% Ni:CZO were prepared by CP/MSS with a reaction time of 6 h in air at 650 °C. The diffraction peaks of both powders (Figure 1a) were indexed to cubic $(Ce_{0.69}Zr_{0.31})O_2$ (ICSD 157416)[57] with no Ni or NiO peaks detected. The lattice parameters of the CZO and 6.6 mol% Ni:CZO (starting from 10 mol% Ni in the initial solution) NPs were calculated to be 5.31 Å and 5.34 Å, respectively, and are similar to the literature (a = 5.33 Å[57]), with slight expansion upon Ni doping. Crystalline sizes (Scherrer equation) were calculated to be 7.5 nm (CZO) and 8.5 nm (6.6 mol% Ni:CZO), showing that incorporation of Ni slightly increases the size of the NPs (Table 1). The complete XRD results for all CP/MSS samples suggest a homogeneous dispersion of Ni in all samples at the detectability level of XRD (Figure S1). The presence of the signature Ni L_α peak (0.85 keV) from energy dispersive X-ray spectroscopy (EDX) further confirms the presence of Ni in the 6.6 mol% Ni:CZO NPs (Figure 1b). As with the XRD measurements, the BF-STEM images of the 6.6 mol% Ni-doped sample show a slight change of the (222) lattice spacing (d=3 Å, Figure 1c). The size distribution is observed in the inset of Figure 1c for the 6.6 mol% Ni. Figure S2 shows the CZO particle size distribution with and without doping, with negligible changes observed, consistent with the crystallite sizes extracted from XRD. The structural characterization indicates that Ni was incorporated into the lattice with no measurable island formation on the surface. As such, different Ni dopant concentrations of up to 20 mol% in solution were employed to study the effect of dopant concentration on the catalytic

activity. At higher Ni concentrations a blue effluent was seen suggesting the Ni was in excess of the solid solubility limit.[58] Excess Ni/NiO is not believed to deposit on the precipitate surface due to extensive washing of the precipitate which would remove unincorporated Ni-OH.[40] Additionally, the powders had a yellow color instead of a black color which would be expected with NiO formation on the surface. To quantify the Ni concentration and verify the stoichiometry of the catalyst, ICP-OES was performed (Table S1, Supporting Information). A maximum of 9.3 Ni mol% in the catalyst was determined for the initial 20 mol% Ni in solution. While the ICP-OES cannot determine the position of the Ni, it is expected that these islands would be detectable as elevated coking rates during the DRM reaction.

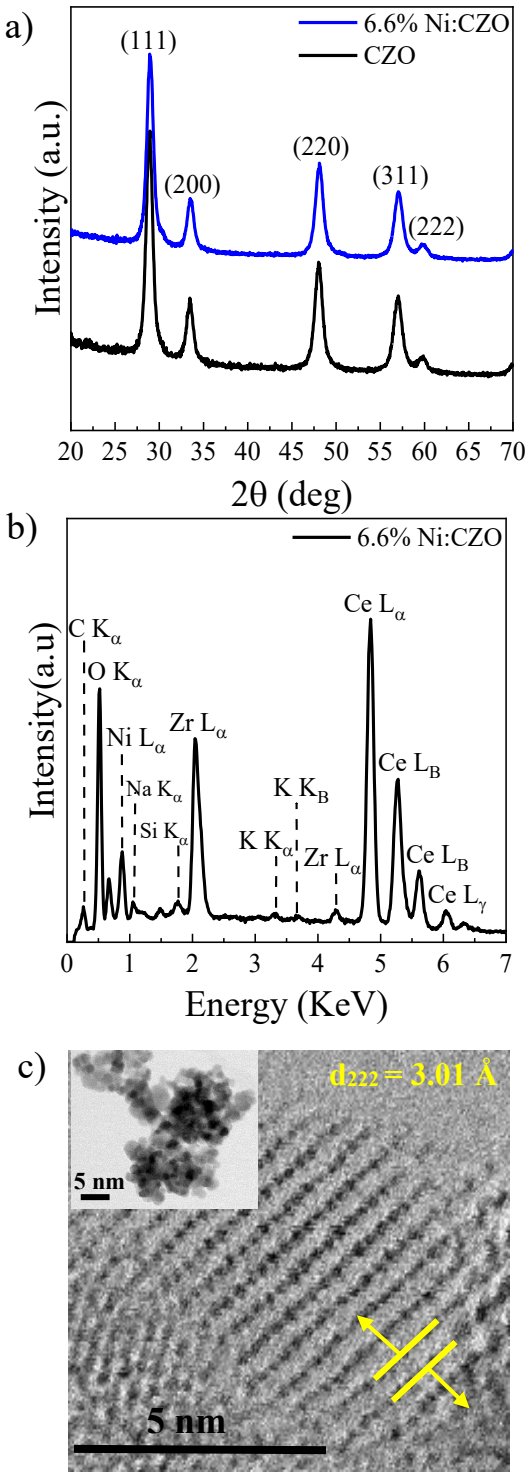

Figure 1. a) XRD of CZO and 6.6 mol% Ni:CZO indicating no phase separation for these NPs. b) EDX confirming the presence of Ni in 6.6 mol% Ni:CZO. c) BF-STEM image of Ni:CZO (6.6 mol%) with observed *d*-spacing of 3.01 Å (d_{222}= 3.05 Å) and HRTEM image in the inset.

The Ni:CZO catalysts doped with Ni during crystallization were compared to a conventionally prepared sol-gel/urea deposition-precipitation (strong electrostatic adsorption) catalyst containing 5 mol% of Ni.[55, 59, 60] Unlike the reference catalyst, small/no phase segregation was observed for the 9.3 mol% Ni:CZO core (Figure 2a). Additionally, *in-situ* doping of the core did not require a pre-catalytic reaction reducing treatment to activate and drive the Ni dopant into the structure which was necessary for the Ni post-deposition. The catalyst activity (rate of the DRM reaction) and coking rates for the samples run at differential conversion in the DSC/TGA are shown in Table 1. The heating rate is directly proportional to the DRM reaction rate. The DRM rate on a weight basis can be calculated using a process simulator (Aspen HYSYS) from the heat rate. While the reverse water-gas shift is present in the fixed bed reactor, this side reaction is not considered in the simulation as its nearly thermoneutral nature would not affect the overall heat flux. The reference catalyst exhibited a higher reforming rate on a weight basis. When normalized to surface area, the 4.6 and 6.6 mol% Ni:CZO showed reduced activity compared to the reference, despite similar Ni

Table 1. Effect of increased Ni doping (mol%) on particle size, estimated oxygen vacancy concentrations (*N*) and catalytic activity. The activities are normalized to the surface area.

Sample	Size[a] (nm)	Surface area (m^2/g)	N^b (cm^{-3})	$[O_{III}]^c$ (%)	Activity (mW/m^2)	Coking rate ($mg_{coke}/m^2 \cdot h$)	Reforming rate ($mmol/m^2 \cdot h$)
CeO_2 (sol-gel)	-	219	-	-	$7x10^{-3}$	-	-
CZO (sol-gel)	-	183	-	-	0.01	-	-
CZO	7.9	38	$6.3x10^{21}$	5.32	0.01	-	-
Reference	5.1	77	$7.9x10^{21}$	-	0.12	$1.04x10^{-5}$	1.69
4.6% Ni	8.2	38	$9.9x10^{21}$	7.85	0.03	$1.76x10^{-6}$	0.87
6.6% Ni	8.5	33	$1.2x10^{22}$	11.19	0.05	$7.27x10^{-7}$	1.64
9.3% Ni	9.2	32	$3.8x10^{22}$	19.79	0.13	$3.75x10^{-6}$	2.56
Core (4.6 mol%) - shell (2 wt%)	9.9	15	$2.3x10^{22}$	17.36	0.57	$3.4x10^{-6}$	8.67

[a] Extracted crystalline size from XRD spectra.
[b] Estimated oxygen vacancy site concentration, details in Calculation 1.
[c] Extracted from deconvoluted O 1*s* XPS peaks.

concentrations to that of the reference catalyst. However, the 9.3 mol% Ni:CZO catalysts is comparable to the reference catalyst, but more importantly, the coking rate was 85% less with the subsurface Ni inclusion.

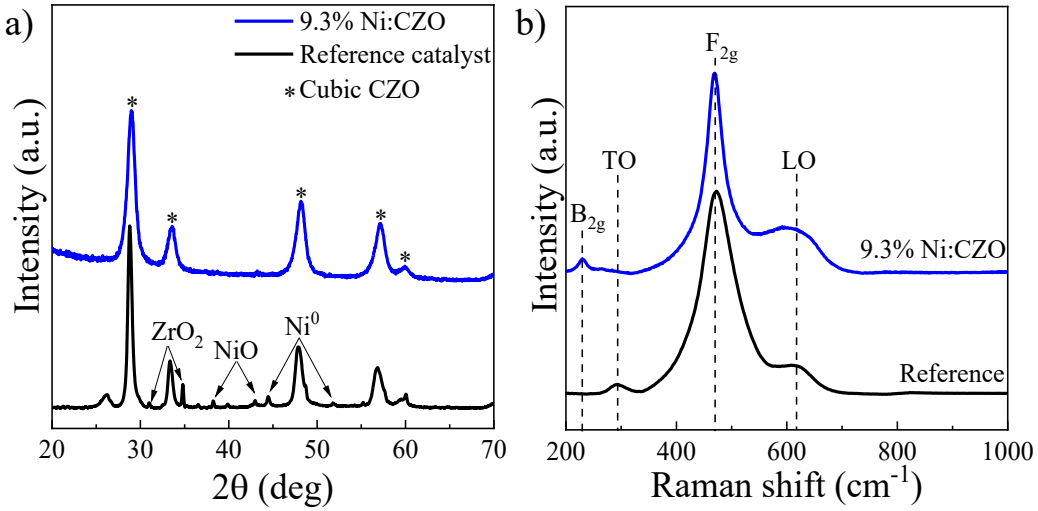

Figure 2. (a) XRD of 9.3 mol% Ni:CZO and the reference catalyst showing greater phase separation for Ni and ZrO_2 in the reference catalyst. (b) Raman spectra showing an increase in the area of the LO band for the 9.3 mol% Ni:CZO compared to the reference catalyst.

To test the activity and stability of the 9.3% CP/MSS catalyst at higher partial pressures and conversions, a longer-term (1 day) fixed bed reactor test at 750 °C was performed (Table 2). The CH_4 conversion × GHSV (an activity metric) of the reference catalyst was ~ 8250 mL/min×g vs. 6800 mL/min×g for the 9.3 mol% Ni:CZO. The ratio of H_2/CO of the 9.3 mol% Ni:CZO was 0.44, slightly higher than the reference catalyst (0.42), suggesting a slight decrease, but still considerable, RWGS.[61]

Incorporation of Ni into the bulk lattice, as would more likely occur with the 9.3 mol% Ni:CZO catalyst, is believed to result in more oxygen vacancies (and higher OSC) due to the difference in the oxidation states of the Ni and Zr.[62] The vacancies act as sites where active oxygens can be stored and released, mitigating carbon polymerization. This effect could be responsible for the decreased coking rate of the 9.3 mol% sample. However, the results also suggest that dopant incorporation during crystal growth may not distribute enough Ni at particle surfaces where it is needed to catalyze the DRM reaction. This lower Ni concentration and overall decrease in surface area are responsible for the slightly lower CH_4 and CO_2 conversions.

Table 2. Fixed-bed reactor data for the 9.3 mol% Ni:CZO.

Catalyst	H_2/CO ratio	CH_4 Conversion×GHSV (mL/min×g)	CO_2 Conversion (%)
Reference	0.42	8250	29.2
9.3% Ni:CZO	0.44	6800	24.4

To better understand the effect of Ni location on the catalysis, Raman spectroscopy was performed on the reference and 9.3 mol% samples (Figure 2b). Three characteristic regions of interest, around 228, 470, and 615 cm^{-1}, are attributed to vibrations of Zr-O bonds (symmetrical stretching, B_{2g} mode), Ce-O bonds (symmetrical stretching, F_{2g} mode), and a defect-induced (LO) phonon band, respectively.[63] The blue-shift (474 to 470 cm^{-1}) in the F_{2g} band of the 9.3 mol% Ni is attributed to an increase in the bond length of Ce-O caused by Ni incorporation, consistent with its smaller ionic radius compared to Zr^{4+}.[64] Additionally, the change in intensities of the F_{2g} and LO bands are indicative of oxygen vacancy incorporation.[65] The oxygen vacancy concentrations were estimated using a correlation length model for the F_{2g} band (Supporting Information, Calculation 1).[66, 67] The estimated oxygen vacancy concentration (N) for the 9.3 mol% Ni:CZO catalyst is approximately 5 times more than the reference catalyst (Table 1), suggesting greater

Ni^{2+} incorporation in the lattice induces more oxygen vacancies. Therefore, it is reasonable to conclude that the reduced coking rates of the CP/MSS catalysts result from the higher oxygen vacancy concentrations characteristic of this synthesis/structure. When comparing two materials of similar Ni concentrations, 4.6 mol% Ni:CZO vs. the reference, the increase in oxygen vacancy concentration is 25% while the reforming rate is reduced by 75%, suggesting the Ni is preferentially located below the catalyst surface at lower concentrations.

The formation of oxygen vacancies is one of the important characteristics of doped Ni:CZO, with incorporation of Ni within the bulk lattice improving the OSC.[18, 47] Figure 3 shows that the area under the LO band at 615 cm^{-1} increases proportional to the Ni concentration, indicating that more Ni creates more oxygen vacancies within the lattice (Table 1). Along this line, it is significant that a single XRD-detectable phase is maintained for Ni:CZO NPs even with a substantial increase in Ni content, implying a uniform dispersion throughout the particle (Figure S1). However, due to the nature of the crystallization process, eventually thermodynamics dictates that the Ni will segregate to the nanoparticle interface.

To further quantify the Ni dispersion, CO absorption was performed on the Ni:CZO samples (Table S2). As expected, the amount of CO chemisorbed to the surface increased proportionally with Ni concentration. The increased DRM activities are attributed to the improved Ni surface dispersion. The MSS synthesized samples all exhibit activities of $3x10^{-4}$ mW/mol exposed Ni. Since both oxygen vacancies and surface Ni are important for enhancing the CO_2 activation step of the DRM reaction[68-70], it is not surprising that the 9.3 mol% Ni:CZO catalyst shows the highest reforming rate (2.56 mmol/m^2×h) among the three CP/MSS catalysts. Similar effects are seen with traditional methods and have been ascribed to Ni^{2+} migration from the lattice during the reduction steps.[47, 71, 72] Therefore, incorporation of Ni during the CZO crystallization

can result in a more stable structure, reducing post-synthetic phase segregation and Ni diffusion, which was observed for the reference catalyst under reducing enviroments.[45] Furthermore, the subsurface Ni can help mobilize the bulk oxygen via Ce-O bond stress, allowing for oxygen migration toward the surface and reducing coking rates [23, 72-74]

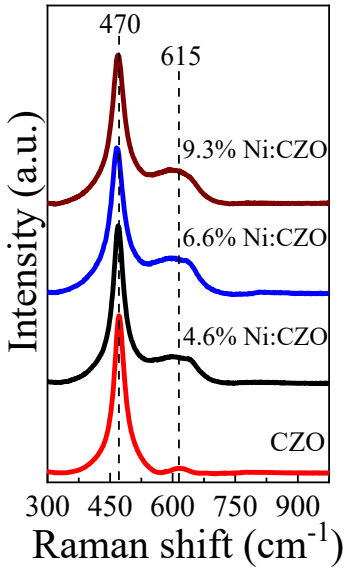

Figure 3. Raman spectra for the CP/MSS particles with increasing Ni contents. The spectra show an increase in the ratio of peak intensities I_{LO}/I_{F2g}.

To observe the change in electronic state of oxygen and cerium at different Ni concentrations, XPS measurements were performed (Figure 4). The O 1*s* spectra can be deconvoluted into four peaks: (1) oxygen ions associated with 2^- formal charge or oxygen double bonded to carbon (O=C) (O_I) at ~ 528.8 eV, (2) lattice oxygen (O_{II}) at ~ 530.5 eV, (3) a shoulder peak (O_{III}) at ~ 531.15 eV indicative of nearby oxygen vacancies, (4) oxygen in surface hydroxyl groups, adsorbed H_2O, or surface -CO_3 (O_{IV}) at ~ 532.44 eV.[75-77] Table 1 shows the calculated percentages of the oxygen vacancies (O_{III}) are 9.9, 17, 24, and 32%, corresponding to CZO, 4.6 mol% Ni:CZO, 6.6 mol% Ni:CZO, and 9.3 mol% Ni:CZO, respectively, denoting an increase in undercoordinated Ce (increased oxygen vacancies), consistent with the Raman measurements.[40, 77] To further confirm this peak is attributable to the oxygen vacancies, adsorbed surface species

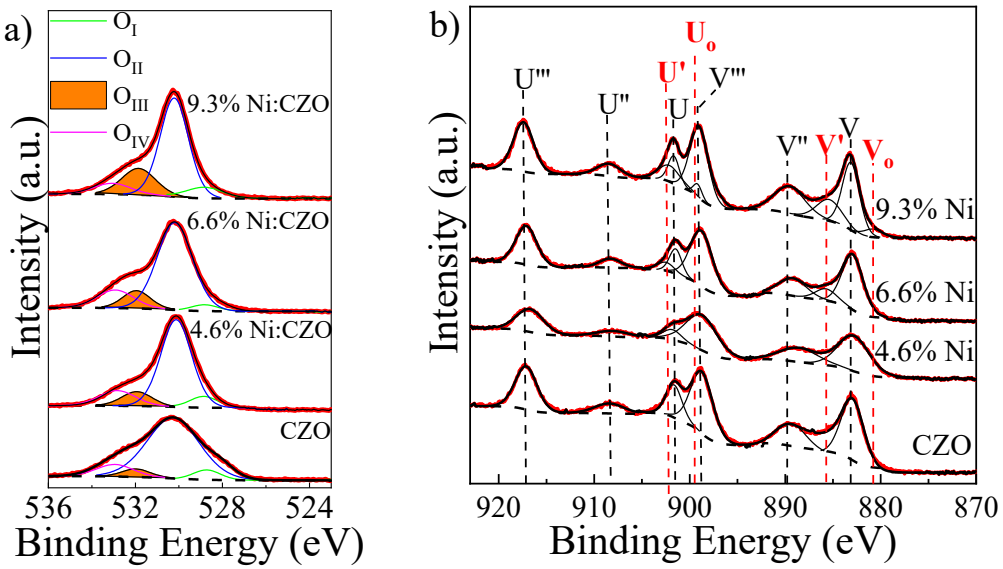

Figure 4. (a) XPS of the O 1*s* region showing an increase in the area of oxide ions with an increase in Ni doping. (b) Ce 3*d* XPS spectra of CZO with 4.6, 6.6, and 9.3 mol% Ni, displaying an increase in the peak areas U_o, U', V_o, and V', all of which correspond to Ce^{3+}, with respect to Ni content.

were removed via air and vacuum annealing (T = 600 °C) from the 9.3% Ni:CZO (Figure S3a). While annealing the sample in air slightly reduced the intensity of the O_{IV} peak, the overall effect is essentially negligible. However, complete removal of surface species was achieved with vacuum annealing along with a slight increase in the O_{III} peak, as expected (Table S3).[78, 79] To further confirm the intrinsic oxygen vacancies and remove the surface contaminants in the remaining samples, gentle sputtering was performed (Figure S3b) with Ar^+ ion bombardment for 10 min. After sputtering, the complete removal of O_I and O_{IV} peaks is observed, with the O_{III} peak following the same trend as the non-sputtered samples (Table S3). These results are also corroborated by the Ce 3*d* XPS spectra (Figure 4b). Peaks *V* and *U* are related to the spin-orbit splitting of Ce $3d_{5/2}$ and Ce $3d_{3/2}$, respectively. The deconvoluted peaks labeled as U''', U'', U, V''', V'', V correspond to the $3d^{10}4f^0$ state of Ce^{4+} while U_o, U', V_o, and V', marked as red, correspond to $3d^{10}4f^1$ state of Ce^{3+}.[80] It is evident that the concentration of Ce^{3+} and oxygen vacancies are

directly proportional to the Ni^{2+} concentration.[81-83] The fraction of Ce^{3+} near the surface of the catalysts was calculated for each sample (Supporting Information, Calculation 2).[84] The calculation shows that 6.6% Ni:CZO and 9.3% Ni:CZO have 8.65% and 16.67% Ce^{3+} oxidation state present. The evolution of Ce^{3+}, the increase in the area of O_{III} and of the Raman LO peak all confirm that Ni incorporation increases the number of oxygen vacancies in the catalyst.

A final confirmation of the increase in oxygen vacancy concentrations with respect to Ni incorporation can be intuited from TPR measurements starting from a fully oxidized (500°C, air, 1 h) catalyst (Figure S5). The results, summarized in Table S4, show three reduction peaks for all the catalysts, with a small fourth one (from ~587-666°C) also discernible for the 9.3 mol% sample. The lowest temperature peak can be ascribed to surface adsorbate removal and facile reduction of surface NiO,[70, 85-89] and the highest temperature peak to bulk reduction of Ce^{4+} not affected by Ni or Zr.[60, 90-92] The other peak(s) can all be attributed to reduction of subsurface Ni^{2+} and reduction of Ce^{4+} (with formation of new oxygen vacancies) that is associated with dispersed Ni^{2+} and Zr^{4+} in the distorted fluorite structure.[70, 85-89, 91, 93] There is no separate peak for the MSS samples that can be ascribed to bulk NiO (whose maximum is usually at 420-455°C),[60, 90-92] but there is a lower temperature shoulder present, including for CZO itself. The temperature range of this broad peak extends to lower temperatures as the amount of Ni increases from 0 to 9.3 mol%, because there are more easily reducible sites (near the surface, associated with Ni^{2+}), but the total amounts reduced within this broad peak decrease as a percentage of the total possible theoretical reduction amounts. These results suggest that with more Ni present, there is also more subsurface Ni^{2+}, and this subsurface population is harder to extract and reduce. Note from Table S4 that the only two samples undergoing almost complete theoretical reduction to Ni^0 and Ce_2O_3 at 1000 °C are CZO and the core-shell sample, the first without Ni and the second with a high percentage of surface

Ni. Finally, the weight recoveries were all >99% except for the 9.3 mol% sample (98.3%), which suggests that for a high Ni concentration some permanent reduction to larger Ni^0 aggregates also took place. But the overall picture is that of concomitant reduction of some Ni^{2+} and some Ce^{4+} over the most relevant temperature range.

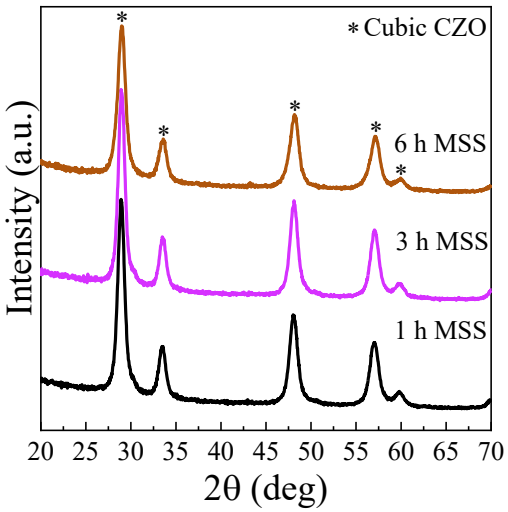

Figure 5. XRD measurements of 20% Ni:CZO after 1, 3, and 6 h synthesis reaction times show only the cubic CZO structure.

Based on the above observations, controlling both the oxygen vacancy concentrations and the Ni distribution between surface and bulk can be considered to be important aspects of the synthesis of active, stable DRM catalysts. To further investigate these phenomena, the crystallization (synthesis) time of the 9.3 mol% Ni:CZO was varied to spot any change in the oxygen vacancy concentrations and coking rates of the NPs (Figure 5). The time of the MSS reaction step is a major factor affecting particle agglomeration and crystallization,[46] which in turn can affect the location and concentration of oxygen vacancies. As seen in Table 3, three different reaction times of the MSS crystallization (1, 3, and 6 h) were tested. The homogeneity of the NPs was maintained (Figure S4). Figure 5 displays a red shift in the F_{2g} band of the 9.3 mol% Ni:CZO as the molten salt reaction time is decreased, corresponding to decreased lattice strain.[94, 95] Greater lattice strain causes a weakening of the Ce-O bonds in the lattice which is caused by incorporation

of Ni in the lattice,[96-98] and is symptomatic of increasing oxygen vacancy concentrations (Table 3). As expected, the coking rate is directly affected, whereas DRM activity is constant with respect to the surface area. However, the trend is the opposite of what might be expected, with higher coking rates associated with the shorter crystallization periods and less lattice strain. This inverse response is attributed to poorer Ni homogeneity and nanocrystal quality at short MSS crystallization times.[46, 99] Specifically, the increase in MSS crystallization time engenders a better Ni rearrangement within the crystal thus causing a lower coking rate for the catalyst.[97, 99]

Table 3. Effects of MSS reaction time on estimated oxygen vacancy concentration and catalytic activity for the 9.3 mol% Ni:CZO.

Molten salt time (h)	Size (nm)	Surface area (m^2/g)	N (cm^{-3})	Catalytic activity (mW/m^2)	Coking rate (mg coke/mg cat·h)
1	7.8	40	5.2×10^{22}	0.13	3.0×10^{-4}
3	8.7	37	4.8×10^{22}	0.13	2.8×10^{-4}
6	9.2	32	3.8×10^{22}	0.13	1.2×10^{-4}

Based on the above results, it was believed that higher DRM activity catalysts could be achieved by simultaneously controlling the oxygen vacancy concentration and surface dispersion/concentration. To test this, a hierarchical core-shell catalyst was synthesized by depositing Ni on the surface of the CP/MSS nanoparticles. For this process, the 4.6 mol% Ni-doped catalyst was selected as a core and coated with an additional 2 wt% Ni via the deposition-precipitation method (~4 wt% total) to mimic the ~5 wt% reference system. A 5% H_2/N_2 treatment at 750 °C was required to activate the Ni dopants, similar to the reference sample. The 4.6 mol% core was chosen due its lack of Ni surface clusters (low surface dispersion). The low Ni concentration was important to limit additional deposition onto pre-existing Ni surface sites to prevent facet formation where coking occurs. While slight Zr segregation is observed after the reduction treatment (Figure S6a), the particles appear more homogeneous than the used reference

sample. Additionally, the shell deposition process increases the total oxygen vacancies based on both Raman (Figure S6b) and XPS (Table 1) characterization methods compared to the core and reference. One drawback that was observed is the decrease in overall surface area which may indicate too high of a Ni concentration during the deposition.

The core-shell catalyst was run under DRM conditions (Table 1) and resulted in a comparable activity on a weight basis compared to the reference catalyst, despite the five-fold smaller surface area. The DRM rate is nearly five times that of the reference catalyst prepared by adsorptive deposition when normalized by surface area and an order of magnitude higher than the MSS particles when normalized by dispersion. The methane conversion for the core-shell catalyst is comparable to values reported in literature based on the catalyst mass ($3.75x10^{-5}$ $mol.g_{cat}^{-1}.s^{-1}$) but shows at least a two-fold increase based on Ni mass ($7.5\ x10^{-5}$ $mol.g_{Ni}^{-1}.s^{-1}$).[3, 100] More importantly, the coking rate of the core-shell catalyst is an order of magnitude lower. The increase in performance is attributed both to the increased number of oxygen vacancies and more dispersed Ni the surface, both of which should facilitate rapid removal of nascent carbon.[101] While more catalyst optimization is needed, the hierarchical structure clearly demonstrates the importance of subsurface and surface Ni doping in methane reformation. Furthermore, it is believed that the type of dopant can be varied to engineer the electronic states and adsorbate-catalyst interaction in line with d-band theory.

4. CONCLUSIONS

In summary, ~20 nm Ni:CZO NPs with Ni doping up to ~10 mol% were synthesized using a two-step CP/MSS method to study the effect of Ni position on structure, oxygen vacancy concentrations, and DRM catalytic activity. This synthesis process produced homogeneous cubic CZO ($Ce_{0.69}Zr_{0.31}$) with Ni concentrations as high as 9.3 mol% with no Ni/NiO island formation

identified via XRD or HRTEM characterization. Additionally, Ni inclusion resulted in the formation of oxygen vacancies proportional to the concentration of subsurface Ni dopants. However, increased oxygen vacancies must be accompanied by a homogeneous Ni distribution in order to achieve the reduced coking rates. The homogenous distribution and enhanced oxygen vacancies are possible due to incorporation of Ni within the CZO crystallization process instead of through a secondary process to drive deposited ions below the surface. This knowledge was used to design a core-shell structure by coupling the MSS method to a Ni-urea adsorptive deposition process to simultaneously engineer greater oxygen vacancy concentration and a better surface-bulk Ni distribution. The core-shell synthetic strategy greatly increased the DRM activity and decreased the coking rate by over an order of magnitude compared to a conventionally prepared Ni:CZO catalyst despite a much lower surface area. This ability to control the content of oxygen vacancies in the host lattice and homogeneously disperse Ni sites in the bulk will prove beneficial in designing stable catalysts with higher activity for methane reformation, among other related reactions. Finally, this method can allow for the spatial control of multiple dopant types, which is very difficult when using a single deposition step.

ASSOCIATED CONTENT

AUTHOR INFORMATION

Corresponding Author

*Email: jamesdorman@lsu.edu.

Author Contributions

B.S. performed the synthesis of the Ni:CZO nanoparticle samples, and completed the XRD, Raman, and XPS analysis. Y.W. assisted with the synthesis of Ni:CZO and XPS analysis. P.D.

performed the SEM/EDX and XPS measurements. C.J. assisted with Raman spectroscopy analysis and TGA-DSC measurements. D.A.C. performed the TEM measurements. C.R. performed and helped analyze the TPR measurements. K.M.D. contributed to major points in the article and assisted with BET measurements. J.A.D. conceived the project and contributed to major points in the article.

Notes

The authors declare no competing financial interest.

§ Supporting Information

The supporting information includes: oxygen vacancy and $Ce^{3+/4+}$ ratio calculations, and detailed characterization (XRD, XPS, HRTEM, ICP-OES, Chemisorption, and TPR-H_2) for the various catalyst structures.

ACKNOWLEDGMENTS

B.S. acknowledges the fellowship support from the Louisiana State University-College of Engineering. P.D. acknowledges the Louisiana Board of Regents (LEQSF(2016-19)-RD-A-03) and U.S. Department of Energy (DOE) under EPSCOR grant no. DE-SC0012432 for financial support. The authors also acknowledge the National Science Foundation (NSF) under Grant No. CHE-1709902 (JAD) and CBET-1510435 (KD) for financial support. STEM analysis was conducted at the Center for Nanophase Materials Sciences, which is a DOE Office of Science User Facility. The authors would like to thank Tochukwu Ofoegbuna for the XRD measurements.

REFRENCES

1. Rostrup-Nielsen, J.; Trimm, D. L., Mechanisms of carbon formation on nickel-containing catalysts. *J. Catal.* **1977,** *48*, 155-165.
2. Roh, H.-S.; Potdar, H.; Jun, K.-W.; Kim, J.-W.; Oh, Y.-S., Carbon dioxide reforming of methane over Ni incorporated into Ce–ZrO_2 catalysts. *Appl. Catal., A* **2004,** *276*, 231-239.
3. Liu, W.; Li, L.; Zhang, X.; Wang, Z.; Wang, X.; Peng, H., Design of Ni-ZrO_2@SiO_2 catalyst with ultra-high sintering and coking resistance for dry reforming of methane to prepare syngas. *J. CO_2 Utilization* **2018,** *27*, 297-307.
4. Li, P.; Chen, X.; Li, Y.; Schwank, J. W., A review on oxygen storage capacity of CeO_2-based materials: Influence factors, measurement techniques, and applications in reactions related to catalytic automotive emissions control. *Catal. Today* **2019,** *327*, 90-115.
5. Zhang, W.; Liu, B.; Zhan, Y.; Tian, Y., Syngas Production via CO_2 Reforming of Methane over Sm_2O_3−La_2O_3-Supported Ni Catalyst. *Ind. Eng. Chem. Res.* **2009,** *48*, 7498-7504.
6. Laosiripojana, N.; Assabumrungrat, S., Methane steam reforming over Ni/Ce–ZrO_2 catalyst: Influences of Ce–ZrO_2 support on reactivity, resistance toward carbon formation, and intrinsic reaction kinetics. *Appl. Catal., A* **2005,** *290*, 200-211.
7. Koubaissy, B.; Pietraszek, A.; Roger, A.; Kiennemann, A., CO_2 reforming of methane over Ce-Zr-Ni-Me mixed catalysts. *Catal. Today* **2010,** *157*, 436-439.
8. Carrasco, J.; López-Durán, D.; Liu, Z.; Duchoň, T.; Evans, J.; Senanayake, S. D.; Crumlin, E. J.; Matolín, V.; Rodríguez, J. A.; Ganduglia-Pirovano, M. V., In situ and theoretical studies for the dissociation of water on an active Ni/CeO_2 catalyst: Importance of Strong Metal–Support Interactions for the Cleavage of O–H Bonds. *Angew. Chem. Int. Ed.* **2015,** *54*, 3917-3921.
9. Xu, S.; Wang, X., Highly active and coking resistant Ni/CeO_2–ZrO_2 catalyst for partial oxidation of methane. *Fuel* **2005,** *84*, 563-567.
10. Xu, W.; Liu, Z.; Johnston-Peck, A. C.; Senanayake, S. D.; Zhou, G.; Stacchiola, D.; Stach, E. A.; Rodriguez, J. A., Steam reforming of ethanol on Ni/CeO_2: reaction pathway and interaction between Ni and the CeO2 support. *ACS Catal.* **2013,** *3*, 975-984.
11. Fornasiero, P.; Balducci, G.; Di Monte, R.; Kašpar, J.; Sergo, V.; Gubitosa, G.; Ferrero, A.; Graziani, M., Modification of the redox behaviour of CeO_2 Induced by structural doping with ZrO_2. *J. Catal.* **1996,** *164*, 173-183.
12. Montini, T.; Melchionna, M.; Monai, M.; Fornasiero, P., Fundamentals and Catalytic Applications of CeO_2-Based Materials. *Chem. Rev.* **2016,** *116*, 5987-6041.
13. Zinkevich, M.; Djurovic, D.; Aldinger, F., Thermodynamic modelling of the cerium–oxygen system. *Solid State Ionics* **2006,** *177*, 989-1001.
14. Bulfin, B.; Lowe, A.; Keogh, K.; Murphy, B.; Lubben, O.; Krasnikov, S.; Shvets, I., Analytical model of CeO_2 oxidation and reduction. *J. Phys. Chem. C* **2013,** *117*, 24129-24137.
15. Zhou, G.; Shah, P. R.; Kim, T.; Fornasiero, P.; Gorte, R. J., Oxidation entropies and enthalpies of ceria–zirconia solid solutions. *Catal. Today* **2007,** *123*, 86-93.
16. Kim, T.; Vohs, J. M.; Gorte, R. J., Thermodynamic investigation of the redox properties of ceria− zirconia solid solutions. *Ind. Eng. Chem. Res.* **2006,** *45*, 5561-5565.
17. Mogensen, M.; Sammes, N. M.; Tompsett, G. A., Physical, chemical and electrochemical properties of pure and doped ceria. *Solid State Ionics* **2000,** *129*, 63-94.
18. Skorodumova, N.; Simak, S.; Lundqvist, B. I.; Abrikosov, I.; Johansson, B., Quantum origin of the oxygen storage capability of ceria. *Phys. Rev. Lett.* **2002,** *89*, 166601.
19. Kim, G., Ceria-promoted three-way catalysts for auto exhaust emission control. *Ind. Eng. Chem. Prod. Res. Develop.* **1982,** *21*, 267-274.

20. Laosiripojana, N.; Assabumrungrat, S., Catalytic dry reforming of methane over high surface area ceria. *Appl. Catal., B* **2005,** *60*, 107-116.
21. Sokefun, Y. O.; Joseph, B.; Kuhn, J. N., Impact of Ni and Mg Loadings on Dry Reforming Performance of Pt/Ceria-Zirconia Catalysts. *Ind. Eng. Chem. Res.* **2019,** *58*, 9322-9330.
22. Li, Y.; Fu, Q.; Flytzani-Stephanopoulos, M., Low-temperature water-gas shift reaction over Cu-and Ni-loaded cerium oxide catalysts. *Appl. Catal., B* **2000,** *27*, 179-191.
23. Theofanidis, S. A.; Galvita, V. V.; Poelman, H.; Marin, G. B., Enhanced carbon-resistant dry reforming Fe-Ni catalyst: Role of Fe. *Acs Catalysis* **2015,** *5*, 3028-3039.
24. Wang, S.; Lu, G.; Millar, G. J., Carbon dioxide reforming of methane to produce synthesis gas over metal-supported catalysts: state of the art. *Energy Fuels* **1996,** *10*, 896-904.
25. Rogers, J. L.; Mangarella, M. C.; D'Amico, A. D.; Gallagher, J. R.; Dutzer, M. R.; Stavitski, E.; Miller, J. T.; Sievers, C., Differences in the nature of active sites for methane dry reforming and methane steam reforming over nickel aluminate catalysts. *ACS Catal.* **2016,** *6*, 5873-5886.
26. Nandini, A.; Pant, K.; Dhingra, S., Kinetic study of the catalytic carbon dioxide reforming of methane to synthesis gas over Ni-K/CeO_2-Al_2O_3 catalyst. *Appl. Catal., A* **2006,** *308*, 119-127.
27. Hu, Y. H.; Ruckenstein, E., Catalytic conversion of methane to synthesis gas by partial oxidation and CO_2 reforming. *ChemInform* **2004,** *35*, 297-345
28. Mette, K.; Kühl, S.; Tarasov, A.; Willinger, M. G.; Kröhnert, J.; Wrabetz, S.; Trunschke, A.; Scherzer, M.; Girgsdies, F.; Düdder, H., High-temperature stable Ni nanoparticles for the dry reforming of methane. *ACS Catal.* **2016,** *6*, 7238-7248.
29. Gao, F.; Tang, X.; Yi, H.; Li, J.; Zhao, S.; Wang, J.; Chu, C.; Li, C., Promotional mechanisms of activity and SO_2 tolerance of Co- or Ni-doped MnO_x-CeO_2 catalysts for SCR of NO_x with NH_3 at low temperature. *Chem. Eng. J.l* **2017,** *317*, 20-31.
30. Dooley, K. M.; Liu, D.; Madrid, A. M.; Knopf, F. C., Oxidative desulfurization of diesel with oxygen: Reaction pathways on supported metal and metal oxide catalysts. *Appl. Catal. A* **2013,** *468*, 143-149.
31. Alifanti, M.; Baps, B.; Blangenois, N.; Naud, J.; Grange, P.; Delmon, B., Characterization of CeO_2− ZrO_2 mixed oxides. Comparison of the citrate and sol− gel preparation methods. *Chem. Mater.* **2003,** *15*, 395-403.
32. Stark, W. J.; Maciejewski, M.; Mädler, L.; Pratsinis, S. E.; Baiker, A., Flame-made nanocrystalline ceria/zirconia: structural properties and dynamic oxygen exchange capacity. *J. Catal.* **2003,** *220*, 35-43.
33. Aneggi, E.; Boaro, M.; de Leitenburg, C.; Dolcetti, G.; Trovarelli, A., Insights into the redox properties of ceria-based oxides and their implications in catalysis. *J. Alloys Compd.* **2006,** *408*, 1096-1102.
34. Nagai, Y.; Yamamoto, T.; Tanaka, T.; Yoshida, S.; Nonaka, T.; Okamoto, T.; Suda, A.; Sugiura, M., X-ray absorption fine structure analysis of local structure of CeO_2–ZrO_2 mixed oxides with the same composition ratio (Ce/Zr= 1). *Catal. Today* **2002,** *74*, 225-234.
35. Vlaic, G.; Fornasiero, P.; Geremia, S.; Kašpar, J.; Graziani, M., Relationship between the Zirconia-Promoted reduction in the Rh-loaded $Ce_{0.5}Zr_{0.5}O_2$mixed oxide and the Zr–O local structure. *J. Catal.* **1997,** *168*, 386-392.
36. Di Monte, R.; Kašpar, J., On the role of oxygen storage in three-way catalysis. *Topics Catal.* **2004,** *28*, 47-57.
37. Asencios, Y. J.; Bellido, J. D.; Assaf, E. M., Synthesis of NiO–MgO–ZrO_2 catalysts and their performance in reforming of model biogas. *Appl. Catal., A* **2011,** *397*, 138-144.

38. Sanchez-Dominguez, M.; Liotta, L. F.; Di Carlo, G.; Pantaleo, G.; Venezia, A. M.; Solans, C.; Boutonnet, M., Synthesis of CeO_2, ZrO_2, $Ce_{0.5}Zr_{0.5}O_2$, and TiO_2 nanoparticles by a novel oil-in-water microemulsion reaction method and their use as catalyst support for CO oxidation. *Catal. Today* **2010,** *158*, 35-43.
39. Neagu, D.; Oh, T.-S.; Miller, D. N.; Ménard, H.; Bukhari, S. M.; Gamble, S. R.; Gorte, R. J.; Vohs, J. M.; Irvine, J. T. S., Nano-socketed nickel particles with enhanced coking resistance grown in situ by redox exsolution. *Nature Comm.* **2015,** *6*, 8120.
40. Darapaneni, P.; Moura, N. S.; Harry, D.; Cullen, D. A.; Dooley, K. M.; Dorman, J. A., Effect of Moisture on Dopant Segregation in Solid Hosts. *J. Phys. Chem. C* **2019,** *123*, 12234-12241.
41. Pokhrel, M.; Wahid, K.; Mao, Y., Systematic studies on $RE_2Hf_2O_7$:5% Eu^{3+} (RE= Y, La, Pr, Gd, Er, and Lu) nanoparticles: effects of the A-site RE^{3+} cation and calcination on structure and photoluminescence. *J. Phys. Chem. C* **2016,** *120*, 14828-14839.
42. Pokhrel, M.; Burger, A.; Groza, M.; Mao, Y., Enhance the photoluminescence and radioluminescence of $La_2Zr_2O_7$: Eu^{3+} core nanoparticles by coating with a thin Y_2O_3 shell. *Opt. Mater.* **2017,** *68*, 35-41.
43. Dorman, J. A.; Choi, J. H.; Kuzmanich, G.; Chang, J. P., Elucidating the effects of a rare-earth oxide shell on the luminescence dynamics of Er^{3+}:Y_2O_3 nanoparticles. *J. Phys. Chem. C* **2012,** *116*, 10333-10340.
44. Dorman, J. A.; Choi, J. H.; Kuzmanich, G.; Bargar, J. R.; Chang, J. P., Optimizing the crystal environment through extended x-ray absorption fine structure to increase the luminescent lifetimes of Er^{3+} doped Y_2O_3 nanoparticles. *J. Appl. Phys.* **2012,** *111*, 083529.
45. Mao, Y.; Park, T.-J.; Wong, S. S., Synthesis of classes of ternary metal oxide nanostructures. *Chem. Commun.* **2005,** 46, 5721-5735.
46. Mao, Y.; Guo, X.; Huang, J. Y.; Wang, K. L.; Chang, J. P., Luminescent nanocrystals with $A_2B_2O_7$ composition synthesized by a kinetically modified molten salt method. *J. Phys. Chem. C* **2009,** *113*, 1204-1208.
47. Park, J. H.; Lee, D. H.; Shin, H. S.; Lee, B. K., Transition of the Particle-Growth Mechanism with Temperature Variation in the Molten-Salt Method. *J. Am. Ceram. Soc.* **1996,** *79*, 1130-1132.
48. Yoon, K. H.; Cho, Y. S.; Kang, D. H., Molten salt synthesis of lead-based relaxors. *J. Mater. Sci.* **1998,** *33*, 2977-2984.
49. R Bajgiran, K.; Darapaneni, P.; Melvin, A. T.; Dorman, J. A., Effects of Weak Electric Field on the Photoluminescence Behavior of Bi^{3+}-Doped YVO_4:Eu^{3+} Core–Shell Nanoparticles. *J. Phys. Chem. C* **2019,** *123*, 13027-13035.
50. Elias, J. S.; Risch, M.; Giordano, L.; Mansour, A. N.; Shao-Horn, Y., Structure, Bonding, and Catalytic Activity of Monodisperse, Transition-Metal-Substituted CeO_2 Nanoparticles. *J. Am. Chem. Soc.* **2014,** *136*, 17193-17200.
51. Khan, S.; Cho, H.; Kim, D.; Han, S. S.; Lee, K. H.; Cho, S.-H.; Song, T.; Choi, H., Defect engineering toward strong photocatalysis of Nb-doped anatase TiO_2: Computational predictions and experimental verifications. *Appl. Catal., B* **2017,** *206*, 520-530.
52. Ofoegbuna, T.; Darapaneni, P.; Sahu, S.; Plaisance, C.; Dorman, J. A., Stabilizing the B-site oxidation state in ABO_3 perovskite nanoparticles. *Nanoscale* **2019, 11**, 14303-14311
53. Tang, Z.; Sorensen, C.; Klabunde, K.; Hadjipanayis, G., Preparation of manganese ferrite fine particles from aqueous solution. *J. Colloid Interface Sci.* **1991,** *146*, 38-52.

54. Jiang, C.; Akkullu, M. R.; Li, B.; Davila, J. C.; Janik, M. J.; Dooley, K. M., Rapid screening of ternary rare-earth–Transition metal catalysts for dry reforming of methane and characterization of final structures. *J. Catal.* **2019,** *377*, 332-342.
55. Dooley, K. M.; Kalakota, V.; Adusumilli, S., High-temperature desulfurization of gasifier effluents with rare earth and rare earth/transition metal oxides. *Energy Fuels* **2011,** *25*, 1213-1220.
56. Fairley, N., *CasaXPS Manual 2.3. 15: CasaXPS Processing Software for XPS Spectra*. Casa Software Limited: 2009.
57. Varez, A.; Garcia-Gonzalez, E.; Jolly, J.; Sanz, J., Structural characterization of $Ce_{1-x}Zr_xO_2$ ($0 \leq x \leq 1$) samples prepared at 1650 C by solid state reaction: A combined TEM and XRD study. *J. Eur. Ceram. Soc.* **2007,** *27*, 3677-3682.
58. Barrio, L.; Kubacka, A.; Zhou, G.; Estrella, M.; Martinez-Arias, A.; Hanson, J. C.; Fernandez-Garcia, M.; Rodriguez, J. A., Unusual Physical and Chemical Properties of Ni in $Ce_{1-x}Ni_xO_{2-y}$ Oxides: Structural Characterization and Catalytic Activity for the Water Gas Shift Reaction. *J. Phys. Chem. C* **2010,** *114*, 12689-12697.
59. Rossignol, S.; Madier, Y.; Duprez, D., Preparation of zirconia–ceria materials by soft chemistry. *Catal. Today* **1999,** *50*, 261-270.
60. Sukonket, T.; Khan, A.; Saha, B.; Ibrahim, H.; Tantayanon, S.; Kumar, P.; Idem, R., Influence of the Catalyst Preparation Method, Surfactant Amount, and Steam on CO_2 Reforming of CH_4 over $5Ni/Ce_{0.6}Zr_{0.4}O_2$ Catalysts. *Energy Fuels* **2011,** *25*, 864-877.
61. Jha, A.; Jeong, D.-W.; Lee, Y.-L.; Nah, I. W.; Roh, H.-S., Enhancing the catalytic performance of cobalt oxide by doping on ceria in the high temperature water–gas shift reaction. *RSC Adv.* **2015,** *5*, 103023-103029.
62. Wang, J.; Shen, M.; Wang, J.; Yang, M.; Wang, W.; Ma, J.; Jia, L., Effects of Ni-doping of ceria-based materials on their micro-structures and dynamic oxygen storage and release behaviors. *Catal. Lett.* **2010,** *140*, 38-48.
63. Wang, R.; Mutinda, S. I.; Fang, M., One-pot hydrothermal synthesis and high temperature thermal stability of $Ce_xZr_{1-x}O_2$ nanocrystals. *RSC Adv.* **2013,** *3*, 19508-19514.
64. Li, G.; Smith, R. L.; Inomata, H., Synthesis of Nanoscale $Ce_{1-x}Fe_xO_2$ Solid Solutions via a Low-Temperature Approach. *J. Am. Chem. Soc.* **2001,** *123*, 11091-11092.
65. Li, X.; Ni, C.; Yao, C.; Chen, Z., Development of attapulgite/$Ce_{1-x}Zr_xO_2$ nanocomposite as catalyst for the degradation of methylene blue. *Appl. Catal., B* **2012,** *117*, 118-124.
66. Kosacki, I.; Petrovsky, V.; Anderson, H. U.; Colomban, P., Raman spectroscopy of nanocrystalline ceria and zirconia thin films. *J. Am. Ceram. Soc.* **2002,** *85*, 2646-2650.
67. Trogadas, P.; Parrondo, J.; Ramani, V., CeO_2 surface oxygen vacancy concentration governs in situ free radical scavenging efficacy in polymer electrolytes. *ACS Appl. Mater. Interfaces* **2012,** *4*, 5098-5102.
68. Du, X.; Zhang, D.; Shi, L.; Gao, R.; Zhang, J., Morphology dependence of catalytic properties of Ni/CeO_2 nanostructures for carbon dioxide reforming of methane. *J. Phys. Chem. C* **2012,** *116*, 10009-10016.
69. Múnera, J. F.; Irusta, S.; Cornaglia, L. M.; Lombardo, E. A.; Cesar, D. V.; Schmal, M., Kinetics and reaction pathway of the CO_2 reforming of methane on Rh supported on lanthanum-based solid. *J. Catal.* **2007,** *245*, 25-34.
70. Kambolis, A.; Matralis, H.; Trovarelli, A.; Papadopoulou, C., Ni/CeO_2-ZrO_2 catalysts for the dry reforming of methane. *Appl. Catal. A* **2010,** *377*, 16-26.
71. Pauling, L., Atomic radii and interatomic distances in metals. *J. Am. Chem. Soc.* **1947,** *69*, 542-553.

72. Mamontov, E.; Egami, T.; Brezny, R.; Koranne, M.; Tyagi, S., Lattice defects and oxygen storage capacity of nanocrystalline ceria and ceria-zirconia. *J. Phys. Chem. B* **2000,** *104*, 11110-11116.
73. Sugiura, M., Oxygen storage materials for automotive catalysts: ceria-zirconia solid solutions. *Catal. Surveys Asia* **2003,** *7*, 77-87.
74. Piumetti, M.; Bensaid, S.; Russo, N.; Fino, D., Nanostructured ceria-based catalysts for soot combustion: investigations on the surface sensitivity. *Appl. Catal., B* **2015,** *165*, 742-751.
75. Hsieh, P.-T.; Chen, Y.-C.; Kao, K.-S.; Wang, C.-M., Luminescence mechanism of ZnO thin film investigated by XPS measurement. *Appl. Phys. A* **2008,** *90*, 317-321.
76. Dupin, J.-C.; Gonbeau, D.; Vinatier, P.; Levasseur, A., Systematic XPS studies of metal oxides, hydroxides and peroxides. *Phys. Chem. Chem. Phys.* **2000,** *2*, 1319-1324.
77. Darapaneni, P.; Kizilkaya, O.; Wang, Z.; Dorman, J. A., Weak Field Tuning of Transition-Metal Dopant Hybridization in Solid Hosts. *J. Phys. Chem. C* **2018,** *122*, 22699-22708.
78. Maimaiti, Y.; Nolan, M.; Elliott, S. D., Reduction mechanisms of the CuO (111) surface through surface oxygen vacancy formation and hydrogen adsorption. *Phys. Chem. Chem. Phys.* **2014,** *16*, 3036-3046.
79. Lee, S.; Mettlach, N.; Nguyen, N.; Sun, Y.; White, J., Copper oxide reduction through vacuum annealing. *Appl. Surf. Sci.* **2003,** *206*, 102-109.
80. Liao, X.; Chu, W.; Dai, X.; Pitchon, V., Bimetallic Au–Cu supported on ceria for PROX reaction: Effects of Cu/Au atomic ratios and thermal pretreatments. *Appl. Catal., B* **2013,** *142*, 25-37.
81. Wang, H.-F.; Gong, X.-Q.; Guo, Y.-L.; Guo, Y.; Lu, G. Z.; Hu, P., A model to understand the oxygen vacancy formation in Zr-doped CeO_2: electrostatic interaction and structural relaxation. *J. Phys. Chem. C* **2009,** *113*, 10229-10232.
82. Seo, S.; Lee, M.; Seo, D.; Jeoung, E.; Suh, D.-S.; Joung, Y.; Yoo, I.; Hwang, I.; Kim, S.; Byun, I., Reproducible resistance switching in polycrystalline NiO films. *Appl. Phys. Lett.* **2004,** *85*, 5655-5657.
83. Nolan, M.; Parker, S. C.; Watson, G. W., The electronic structure of oxygen vacancy defects at the low index surfaces of ceria. *Surf. Sci.* **2005,** *595*, 223-232.
84. Hu, Z.; Liu, X.; Meng, D.; Guo, Y.; Guo, Y.; Lu, G., Effect of ceria crystal plane on the physicochemical and catalytic properties of Pd/ceria for CO and propane oxidation. *ACS Catal.* **2016,** *6*, 2265-2279.
85. Löfberg, A.; Guerrero-Caballero, J.; Kane, T.; Rubbens, A.; Jalowiecki-Duhamel, L., Ni/CeO_2 based catalysts as oxygen vectors for the chemical looping dry reforming of methane for syngas production. *Appl. Catal. B* **2017,** *212*, 159-174.
86. Song, C.; Pan, W., Tri-reforming of methane: a novel concept for catalytic production of industrially useful synthesis gas with desired H_2/CO ratios. *Catal. Today* **2004,** *98*, 463-484.
87. Walker, D. M.; Pettit, S. L.; Wolan, J. T.; Kuhn, J. N., Synthesis gas production to desired hydrogen to carbon monoxide ratios by tri-reforming of methane using Ni–MgO–$(Ce,Zr)O_2$ catalysts. *Appl. Catal. A* **2012,** *445-446*, 61-68.
88. Tang, K.; Liu, W.; Li, J.; Guo, J.; Zhang, J.; Wang, S.; Niu, S.; Yang, Y., The Effect of Exposed Facets of Ceria to the Nickel Species in Nickel-Ceria Catalysts and Their Performance in a NO + CO Reaction. *ACS Appl. Mater. Interfaces* **2015,** *7*, 26839−26849.
89. Shan, W.; Fleys, M.; Lapicque, F.; Swierczynski, D.; Kiennemann, A.; Simon, Y.; Marquaire, P.-M., Syngas production from partial oxidation of methane over $Ce_{1-X}Ni_XO_Y$ catalysts prepared by complexation–combustion method. *Appl. Catal. A* **2006,** *311*, 24-33.

90. Dantas, S. C.; Escritori, J. C.; Soares, R. R.; Hori, C. E., Effect of different promoters on Ni/$CeZrO_2$ catalyst for autothermal reforming and partial oxidation of methane. *Chem. Eng. J.* **2010,** *156*, 380-387.
91. Dong, W.-S.; Roh, H.-S.; Jun, K.-W.; Park, S.-E.; Oh, Y.-S., Methane reforming over Ni/Ce-ZrO_2 catalysts: effect of nickel content. *Appl. Catal. A: Gen.* **2002,** *226*, 63-72.
92. Sengupta, P.; Khan, A.; Zahid, M. A.; Ibrahim, H.; Idem, R., Evaluation of the Catalytic Activity of Various 5Ni/$Ce_{0.5}Zr_{0.33}M_{0.17}O_{2-\delta}$ Catalysts for Hydrogen Production by the Steam Reforming of a Mixture of Oxygenated Hydrocarbons. *Energy Fuels* **2012,** *26*, 816-828.
93. Lee, S. M.; Lee, Y. H.; Moon, D. H.; Ahn, J. Y.; Nguyen, D. D.; Chang, S. W.; Kim, S. S., Reaction Mechanism and Catalytic Impact of Ni/CeO_{2-x} Catalyst for Low-Temperature CO_2 Methanation. *Ind. Eng. Chem. Res.* **2019,** *58*, 8656-8662.
94. Sahu, S.; Pandey, S. K.; Manivannan, A.; Deshpande, U. P.; Sathe, V. G.; Reddy, V. R.; Sevi, M., Direct evidence for phase transition in thin $Ge_1Sb_4Te_7$ films using in situ UV–Vis–NIR spectroscopy and Raman scattering studies. *Phys. Status Solidi B* **2016,** *253*, 1069-1075.
95. Lewis, I. R.; Edwards, H., *Handbook of Raman spectroscopy: from the research laboratory to the process line*. CRC Press: 2001.
96. Johansson, B.; Luo, W.; Li, S.; Ahuja, R., Cerium; crystal structure and position in the periodic table. *Sci. Rep.* **2014,** *4*, 6398.
97. McBride, J.; Hass, K.; Poindexter, B.; Weber, W., Raman and x-ray studies of $Ce_{1-x}RE_xO_{2-y}$, where RE= La, Pr, Nd, Eu, Gd, and Tb. *J. Appl. Phys.* **1994,** *76*, 2435-2441.
98. Tiwari, S.; Bajpai, G.; Srivastava, T.; Viswakarma, S.; Shirage, P.; Sen, S.; Biring, S., Effect of strain due to Ni substitution in CeO_2 nanoparticles on optical and mechanical properties. *Scripta Materialia* **2017,** *129*, 84-87.
99. Fano, U., Pressure broadening as a prototype of relaxation. *Phys. Rev.* **1963,** *131*, 259.
100. Zhang, J.; Li, F., Coke-resistant Ni@SiO_2 catalyst for dry reforming of methane. *Appl. Catal. B* **2015,** *176*, 513-521.
101. Li, L.; Feng, X.; Nie, Y.; Chen, S.; Shi, F.; Xiong, K.; Ding, W.; Qi, X.; Hu, J.; Wei, Z., Insight into the effect of oxygen vacancy concentration on the catalytic performance of MnO_2. *ACS Catal.* **2015,** *5*, 4825-4832.

TOC figure

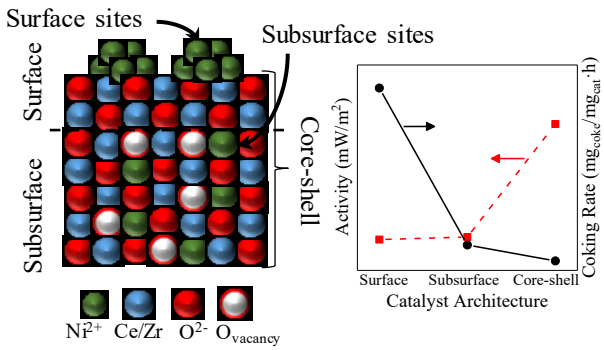
Surface sites
Subsurface sites
Surface
Subsurface
Core-shell
Ni2+ Ce/Zr O2- Ovacancy
Activity (mW/m2)
Coking Rate (mgcoke/mgcat·h)
Surface Subsurface Core-shell
Catalyst Architecture